Enhanced phoretic self-propulsion of active colloids through surface charge asymmetry

Ahis Shrestha [1,2] and Monica Olvera de la Cruz [1,3,2]

[1]*Center for Computation and Theory of Soft Materials, Northwestern University, Evanston, Illinois 60208, USA*
[2]*Department of Physics and Astronomy, Northwestern University, Evanston, Illinois 60208, USA*
[3]*Department of Materials Science and Engineering, Northwestern University, Evanston, Illinois 60208, USA*

Charged colloidal particles propel themselves through asymmetric fluxes of chemically generated ions on their surface. We show that asymmetry in the surface charge distribution provides an additional mode of self-propulsion at the nanoscale for chemically active particles that produce ionic species. Particles of sizes smaller than or comparable to the Debye length achieve directed self-propulsion through surface charge asymmetry even when ionic flux is uniform over its surface. Janus nanoparticles endowed with both surface charge and ionic flux asymmetries result in enhanced propulsion speeds of the order of μm/s or higher. Our work suggests an alternative avenue for specifying surface properties that optimize self-propulsion in ionic media.

I. INTRODUCTION

Many microorganisms exhibit locomotion in viscous fluid environments typically driven by asymmetric surface activity [1,2]. Inspired by such biological systems, micro- and nanomotors have been developed with a wide range of functionalities for targeted cargo transport and various other biomedical or environmental applications [3–5]. Directed motion of colloidal particles has been achieved through externally imposed fields or gradients, as in electrophoresis or diffusiophoresis [6,7]. Alternatively, chemically active colloids, namely, Janus micro- or nanoparticles, self-propel by harnessing locally stored chemical energy [8–10]. Their surface features can be specified to enhance self-propulsion [11–13].

Phoretic active particles propel themselves through a self-generated concentration gradient of solute, a process known as self-diffusiophoresis. Local chemical gradients are generally mediated by surface reactions that induce a nonuniform flux of chemical species, which allows for phoretic movement resulting from the chemical transport in the surrounding fluid [3,10]. Such particles may also have a certain intrinsic surface charge, in concurrence with a flux of ionic species being released or absorbed at the surface. Moreover, the bulk solution itself may have some background ion concentration. In this case an electrostatic contribution arises from the interaction of the charged surface and the mobile ions and couples with ionic transport and hydrodynamics, leading to a different type phoretic motion called ionic self-diffusiophoresis [10,14–20].

In recent years self-propulsion of charged colloidal particles, driven by asymmetric release of ions from their surface, has been realized with micro- and nanomotors, such as urease-powered colloids or photoactivated AgCl Janus particles [13,16,17,21–23]. We demonstrate here that a particle undergoing ionic self-diffusiophoresis (see Fig. 1) attains directed self-propulsion through an asymmetric distribution of surface charge, even when the ionic flux on its surface is uniform. This occurs in regimes where the particle size is smaller than or comparable to the Debye length. In such domains, the near-field electrostatic and hydrodynamic contributions resulting from the asymmetry in surface charge become crucial. Moreover, we find nanosized particles bearing both surface charge and ionic flux asymmetries achieve enhanced self-propulsion with optimal speeds that persist at higher ionic concentrations. The significance of such a transport mechanism at the nanoscale regime is highly relevant to the longstanding efforts in understanding the spatial organization and functionality of subcomponents existing inside the cell [24–28]. In particular, recent experiments investigating bacterial microcompartments (BMCs) have been found to posses chemically active and heterogeneous surface features. BMCs are comprised of a protein shell, which is typically 40–200 nm in size, and facilitates local chemical reactions that produce ionic fluxes at specific sites [29,30]. Their shells are also patterned with distinct protein species that carry different charge, resulting in a nonuniform surface charge, as evident in the icosahedral shells that have been crystallized [31–35]. We hypothesize that the self-propulsion mechanism mediated by surface charge asymmetry will play a role in the chemotactic transport of such microcompartment systems [36]. The effects of surface charge asymmetry on phoretic propulsion speed of active nanoparticles are quantitatively addressed here.

This article is organized as follows. We describe in Sec. II the governing equations and the boundary conditions for the steady state continuum model of ionic self-diffusiophoresis that we use to quantify the propulsion speed. In Sec. III we discuss our results for the case of a particle with asymmetric surface charge but uniform ion flux, and the case of Janus nanoparticles with different configurations of surface charge and ion flux asymmetries. Finally, we provide our concluding remarks in Sec. IV. In addition, we also include supplemental details of our analytic derivations and numerical simulations in the Appendix.
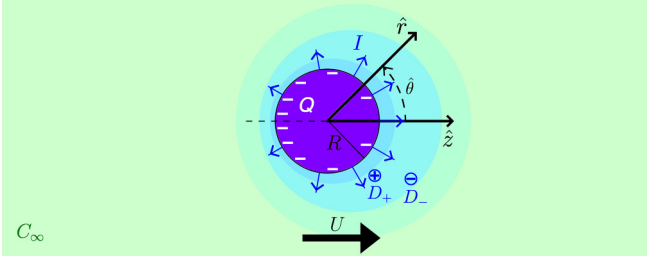
FIG. 1. Schematic of ionic self-diffusiophoresis. A spherical colloidal particle of radius R and net negative charge Q that releases positive and negative ion species at a net rate I from the surface with diffusivities $D_\pm$. The particle has asymmetric distributions of surface charge and ionic flux, and drifts with velocity U in the z direction inside a solution with bulk ion concentration C_∞.

II. CONTINUUM THEORY OF IONIC SELF-DIFFUSIOPHORESIS

We take a continuum approach [17–19,37,38] to characterize the coupling of electrostatics with ionic transport and fluid flow, and determine the particle's phoretic velocity. We consider a spherical particle of radius R with a net charge Q suspended in a solution with total bulk ion concentration C_∞. Through chemical reactions on the surface [16,17], the particle produces different ion species i at a finite constant rate I_i with a sum total rate $I = \sum_i I_i$ (see Fig. 1). We assume the solution is dilute, that is, the ion volume fraction is low such that it is taken as an ideal mixture where the ions diffuse readily with diffusivity D_i. Moreover, we consider the solution to be a linear dielectric medium and treat the interactions between the particle and ions at a continuum mean-field level.

A. Steady-state approximation

We operate under steady state time regimes when the particle is moving with a constant phoretic velocity U in the z direction (see Fig. 1). More specifically, we consider timescales where the Péclet number Pe $\sim RU/D_i$ is low. This means that the local concentration of the ions around the particle adjusts more rapidly than the change in the instantaneous position of the particle due to its propulsion. However, in this work we do not study the effects of Brownian fluctuations on the particle's motion and orientation, which becomes relevant at longer times [10,39,40]. Here we focus our analysis on the propulsive motion during the steady state.

The electrostatic interactions between the charged surface and the ions that are being produced from its surface, as well as the existing background ions, is accounted for by the Poisson equation. Due to the motion of the ions in the resulting electric field, an additional electrochemical flux accompanies the chemical diffusion as prescribed by the Nernst-Planck equations, together written as

$$\nabla^2 \psi = -\frac{e}{\varepsilon} \sum_i Z_i C_i, \qquad \nabla^2 C_i + \frac{eZ_i}{k_B T} \vec{\nabla} \cdot (C_i \vec{\nabla} \psi) = 0, \quad (1)$$

where ψ is the electrostatic potential, e is the elementary charge, ε is the permittivity in water, and C_i is the concentration of the ionic species i with ion valency Z_i. We have excluded the advective term in Eq. (1) since we are in the

low-Pe regime. Moreover, based on the typical solution density and viscosity, and the size and speed of the particles, we also fall under the low-Reynolds-number regime. Henceforth, the flow of the solution, considered as an incompressible fluid, is described using the Stokes equations

$$\vec{\nabla} p - \eta \nabla^2 \vec{v} = \varepsilon \nabla^2 \psi \vec{\nabla} \psi, \qquad \vec{\nabla} \cdot \vec{v} = 0, \qquad (2)$$

where $\vec{v}$ is the fluid velocity, with p the pressure and η the viscosity of water. The electrostatic volume force density comes into Eq. (2) as an applied body force in the fluid maintaining momentum balance [17,18].

We apply the generalized Lorentz reciprocal theorem for Stokes flow with nonzero body force [41–44] to directly calculate the phoretic velocity (see Appendix A). Following previous works [17,18], we find that the phoretic velocity is given by

$$U = \frac{\varepsilon}{6\pi \eta R} \int_V \nabla^2 \psi \vec{\nabla} \psi \cdot (\hat{v} - \hat{z}) \, dV, \qquad (3)$$

where V is the entire fluid volume outside the particle, and $\hat{v}$ is the solution of the Stokes equations with zero body force for a sphere drifting with unit velocity in the positive z direction [17,18]. We note that this general form for U, given by Eq. (3), captures the contributions arising from a finite Debye length relevant for nanosized particles.

B. Surface and bulk conditions

We focus our analysis on a particle that is patterned on its surface with asymmetry in the charge distribution and ion release defined by charge density $\sigma(\theta)$ and ionic flux $j(\theta)$, respectively, which have a polar angle θ dependence with azimuthal symmetry (see Fig. 1). We consider that two distinct monovalent ion species are being generated at the surface, one positive with concentration C_+ and one negative with concentration C_-, as in the case of urease-powered motors where ions NH_4^+ and OH^- are being produced, for instance [17,18]. We assume that both these ions have the same flux pattern $j(\theta)$ at the surface with the same rate of production such that $I_\pm = I/2$; however, they diffuse in the solution with different diffusivity $D_\pm$. While in the background of our solution, we additionally have a 1:1 binary electrolyte, say here Na^+ and Cl^- ions with respective concentrations C_{b+} and C_{b-}.

Moreover, given some finite C_∞, we assume far away from the particle's surface at the bulk, there are many more of the background ion species compared to the ion species that were produced by the particle, such that $C_{b\pm} \to C_\infty/2$ and $C_\pm \to 0$, maintaining electroneutrality with $\psi \to 0$ at the bulk. Furthermore, we have no-slip conditions at the particle surface-solution interface, and the fluid is stagnant at the bulk. Effectively, we have the set of coupled Poisson-Nernst-Planck-Stokes equations (1) and (2) at the steady state, which are subject to the following boundary conditions: (A) $-\varepsilon \vec{\nabla} \psi \cdot \hat{r} = \sigma(\theta)$, $-D_\pm(\vec{\nabla} C_\pm \pm eC_\pm \vec{\nabla} \psi / k_B T) \cdot \hat{r} = j(\theta)$, $(\vec{\nabla} C_{b\pm} \pm eC_{b\pm} \vec{\nabla} \psi / k_B T) \cdot \hat{r} = 0$, and $\vec{v} = U\hat{z}$ all at $r = R$, and (B) $\psi = 0$, $C_\pm = 0$, $C_{b\pm} = C_\infty/2$, and $\vec{v} = 0$ as $r \to \infty$.

C. Small surface charge and ion flux regime

To obtain an analytic approximation for the phoretic velocity, we employ a near-equilibrium perturbation expansion in the Debye-Hückel (DH) limit [17,18]. We consider that the ions being produced by the particle at a steady time is small compared to background ions present in the bulk, and also net charge of the particle is small for a given particle size. In particular, we have $|I| < 2\pi R(D_+ + D_-)C_\infty$ and $|Q| < 4\pi R\varepsilon k_B T/e$. Under these approximations, we can break our problem down into two steps. First step, for the passive ions existing in the background, we treat these background ions such that they are at equilibrium, taking the form of a Boltzmann distribution $C_{b\pm} = C_\infty e^{\mp e\psi/k_B T}/2$. This results in Eq. (1) being written as the modified DH equation, $\varepsilon \nabla^2 \psi \approx e(C_- - C_+) + \varepsilon\kappa^2\psi$, where $\kappa = \sqrt{e^2 C_\infty/\varepsilon k_B T}$. Second step, for the active ions being produced at the particle's surface, we perform a perturbation expansion to approximate an analytical expression in the leading order of I and Q. By expanding $C_\pm$ and ψ in orders of I and Q, we solve the perturbed Eq. (1) with boundary conditions (A) and (B), and we use Eq. (3) to calculate the leading order U (see Appendix B).

III. RESULTS

A. Self-propulsion through surface charge asymmetry

Based on this continuum model, we quantitatively study the phoretic velocity for varied cases of surface asymmetries and bulk ionic strengths. We first examine the scenario in which a particle releases ions uniformly from the surface but has a nonuniform surface charge. In particular, we have a constant flux of $j(\theta) = j_0$, where $j_0 = I/8\pi R^2$ for both the positive and negative ion species, whereas we assume a surface charge distribution in which the charges are more dense on one end of the sphere and then become gradually less dense across the surface towards the opposite end. We consider two configurations: one σ_+ where the charges are more dense on the front ($+\hat{z}$) end, and the other σ_- where charges are more dense on the back ($-\hat{z}$) end. Namely, we defined the two charge densities as $\sigma_\pm(\theta) = \sigma_0(1 \pm \cos\theta)$ with $\sigma_0 = Q/4\pi R^2$ to capture this type of surface charge asymmetry. In this case (see Appendix C), we get the leading order phoretic velocity for charge densities $\sigma_\pm$ as

$$U_{\sigma\pm} = \mp IQ\frac{\alpha}{R} f(\kappa R) + \mathcal{O}(I^2 Q, IQ^2), \tag{4}$$

with $\alpha = e(D_+ - D_-)/16\pi^2 \varepsilon \eta D_+ D_-$ and

$$f(x) = \frac{x^2(x^2 - 12)e^x \text{Ei}(-x) + (x+3)(x^2 - 4x + 2)}{144(x^2 + 2x + 2)}, \tag{5}$$

where Ei is the exponential integral function. We observe that this leading order velocity, that is linear in I and Q, will vanish if the positive and negative ions being released have relatively similar diffusivity as $\alpha \to 0$. Additionally, we see from Eq. (5) that if the particle size is much larger than the Debye length as $\kappa R \gg 1$, $f(\kappa R) \to 0$, also implying a very small vanishing speed. Conversely, when the size of the particle is small compared to the Debye length $1/\kappa$, it acquires larger speeds as $\kappa R << 1$ with $f(\kappa R) \to 1/48$ (see Appendix D). This means that the effect of surface charge asymmetry on

propulsion is significant for nanosized particles with a thick Debye layer.

We show in Fig. 2(a) the analytical DH approximation of the phoretic speed given by Eq. (4) and numerical results for our model performed using finite element (FE) simulations in COMSOL MULTIPHYSICS software (see Appendix E). For instance, given a particle of size $R = 20$ nm, the domain where our DH approximation becomes more accurate is for values of net charge below $|Q^*| \approx 30\, e$ and values of bulk ion concentration above $C_\infty^* \approx 1$ mM for net ion release rates that are below $|I^*| \approx 5 \times 10^8$/s. In this domain we find agreement with the FE results that the speed scales linearly with I and Q, and promptly decreases with an increase in bulk ion concentration C_∞ for a fixed R, as predicted by Eq. (4). We also find $U > 0$ for a particle of net negative charge $Q < 0$ with surface charge density σ_- that is releasing ions with distinct diffusivity such that $D_+ < D_-$, using Eq. (4), in confirmation with FE simulations. This implies that in this case the particle moves in the positive z direction, away from the side with higher charge density [see Fig. 2(b)]. Furthermore, for such parameters used in Fig. 2(a), phoretic speeds of $U \gtrsim 1$ μm/s can be predicted within the DH regime for $\kappa R \lesssim 1$, where the effects of surface charge asymmetry become more prominent.

To gain insight regarding the physical means through which the self-propulsion is being induced here, we need to account for near-field effects [16], especially when the Debye length becomes comparable to particle size. Otherwise, if we only consider the far-field perspective, the system appears to have no asymmetries to cause directed movement as the ion flux is uniform, and consequently, the resulting electric field is symmetric around the particle in this domain beyond the Debye region. Hence in this far-field limit, one would conclude that the particle will have vanishing velocity insufficient to self-propel. On the contrary, we find here that nanosized particles, at bulk ion concentration such that the Debye length becomes proportionate with its size, can move with significant self-propulsion speeds in the order of μm/s or higher, depending on the amount of ion flux and surface charge. The basis of this motion can be understood by looking at the near-field electrostatics that couples to the hydrodynamics. We find that the nonuniform surface charge density produces asymmetric electrostatic potential and electric field as shown in Fig. 2(c). This constitutes an asymmetric electrochemical flux in addition to the uniform diffusive flux, and thus the competing net effect results in a nonuniform ionic distribution around the particle, for instance, as shown in Fig. 2(d) for the released positive ions. This induced ionic gradient gives rise to diffusiophoretic fluid flow near the particle, leading to self-propulsion [3,6,7]. In contrast with propulsion generated only by asymmetric ionic flux [17,18], this asymmetry in surface charge offers an alternative mechanism through which a local concentration gradient is created to mediate self-phoretic motion.

B. Janus nanoparticles with surface charge and ion flux asymmetries

We next explore the effect of combing surface charge asymmetry with ionic flux asymmetry on the phoretic velocity. Firstly, we employ FE simulations to numerically compute
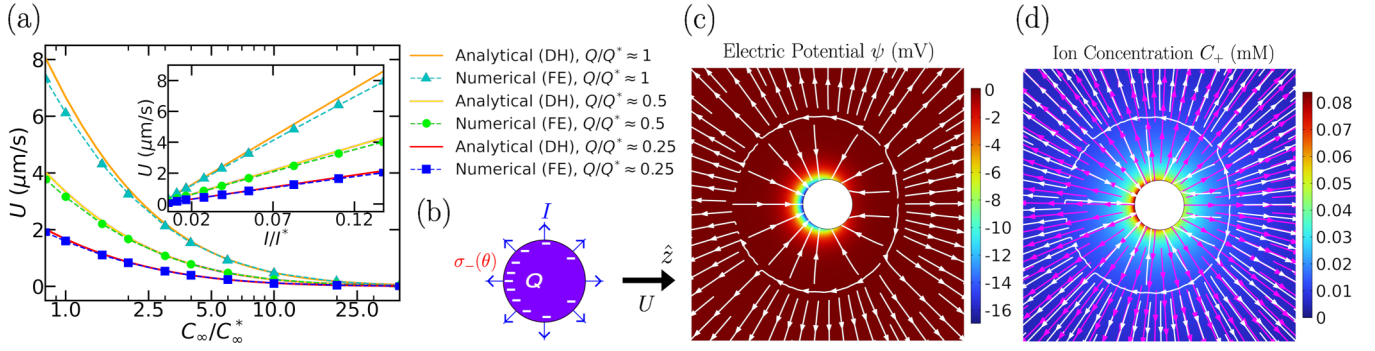
FIG. 2. Self-phoretic motion induced by surface charge asymmetry. (a) The analytical and numerical phoretic speed U as a function of C_∞/C_∞^* for $I/I^* \approx 0.05$, and as a function of I/I^* for $C_\infty/C_\infty^* \approx 2$ (inset), both at the indicated values of Q/Q^*. We use here the leading order near-equilibrium Debye-Hückel (DH) analytical values given by Eq. (4) and the numerical result are from finite element (FE) simulations done in COMSOL MULTIPHYSICS (see Appendix E). (b) Schematic of the particle with uniform ion flux and asymmetric surface charge density $\sigma_-(\theta)$ moving in the $\hat{z}$ direction. The color maps with field lines, from the FE simulations, of (c) the electric potential with electric field and (d) the ion concentration of the positive ion being released C_+ with diffusive (magenta) and electrochemical (white) flux, both for $IQ \approx 0.05\ I^*Q^*$ and $C_\infty \approx C_\infty^*$. In all panels we use $\alpha \approx -0.45\ \mathrm{m^2/C}$, $I^*Q^* \approx -1.5 \times 10^{10} e/\mathrm{s}$, $C_\infty^* \approx 1$ mM, and $R = 20$ nm.

the phoretic velocity of Janus colloids for varying surface charge and ion flux configurations. In particular, we examine four distinct cases of Janus surface charge and ionic flux asymmetries as shown in Fig. 3(a): (i) "Uniform Charge, Janus Flux," where the surface charge density is constant on the whole sphere while the ionic flux is finite on one hemisphere and zero on the other, (ii) "Janus Charge, Uniform Flux," where instead the ionic flux is constant on the whole sphere while the surface charge density is finite on one hemisphere and zero on the other, (iii) "Janus Charge, Janus Flux, Opposite Sides," where on one hemisphere the surface charge density is finite but ionic flux is zero and vice versa on the other, and (iv) "Janus Charge, Janus Flux, Same Side," where the surface charge density and ionic flux are both finite on the same hemisphere and both zero on the other.

We set cases (i)–(iv) such that they all have same I and Q. More specifically, we have the uniform surface charge and ion flux $\sigma(\theta) = \sigma_0$ for case (i) and $j(\theta) = j_0$ for case (ii), respectively. The Janus ion flux for cases (i), (iii)m and (iv) is $j(\theta) = 2j_0$ for $\theta \leqslant \pi/2$ and $j(\theta) = 0$ for $\theta > \pi/2$, while the Janus surface charge for cases (ii) and (iii) is $\sigma(\theta) = 2\sigma_0$ for $\theta \leqslant \pi/2$ and $\sigma(\theta) = 0$ for $\theta > \pi/2$, and vice versa for case (iv).

We compare and contrast the corresponding phoretic velocities of cases (iii) and (iv) with respect to cases (i) and (ii) at different bulk ion concentrations to examine the quantitative differences in phoretic speed resulting from the coupling of surface charge and ion flux asymmetries, and uncover the optimal surface configuration for enhanced self-propulsion. We find that nanoparticles with sizes of $\sim$10–100 nm in solutions
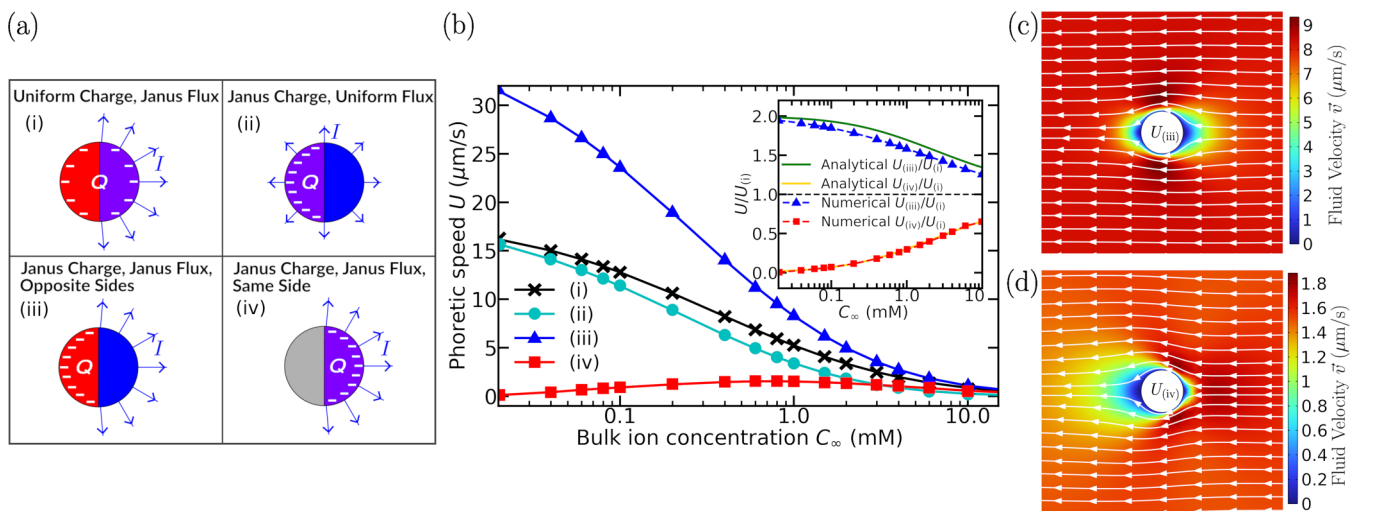

FIG. 3. Enhanced self-propulsion of Janus nanoparticles. (a) Schematic of Janus surface charge and ionic flux configurations (i)–(iv) as described in the text, all with net rate of ions released I and net negative charge Q. (b) The corresponding phoretic speeds U, computed with finite element simulations in COMSOL MULTIPHYSICS (see Appendix E), for the cases (i)–(iv) as a function of bulk ion concentration C_∞. The analytically estimated and numerically computed phoretic speed ratio with respect to case (i), $U/U_{(\mathrm{i})}$, as a function of C_∞ for cases (iii) and (iv) (inset). The color maps and field lines, from FE simulations, of the fluid velocity magnitude and flow direction in the particle's rest frame for (c) case (iii) and (d) case (iv), both at $C_\infty = 1$ mM. In all panels we use $IQ \approx -3.6 \times 10^8 e/\mathrm{s}$, $\alpha \approx -0.45\ \mathrm{m^2/C}$, and $R = 20$ nm.

with bulk ion concentrations of $\lesssim$ 5–50 mM can show speeds that depend on surface configuration. For instance, taking the estimated values of $I \sim 10^7$/s and $Q \sim -10^2$ e based on previous works [17,19], we find differences in speeds of up to ~10 μm/s or higher at bulk ion concentrations <1 mM for a particle of size $R = 20$ nm [see Fig. 3(b)]. In particular, we find case (iii) produces the largest speed that becomes substantially larger with respect to cases (i) and (ii) when $\kappa R \lesssim 1$. We obtain optimally high speeds in this case, which can reach speeds $\gtrsim$ 30 μm/s at very low bulk concentrations $\lesssim$ 0.01 mM, while still maintaining speeds ≈1 μm/s at much higher bulk concentrations, ≈10 mM. In contrast, we find very low speeds for case (iv), which shows a slight increase in speed as bulk concentration is increased (see Fig. 3). For larger nanoparticles, although they move with lower speeds in a regime of lower bulk ion concentration, we find the same behavior with regard to the effect of these surface configurations (see Appendix F). Taken together, this indicates that surface properties such as arrangement of surface charge and ion flux are crucial in regimes where the particle size is below or in the order of the Debye length.

The shifts in the phoretic speeds arising from the surface charge and ionic flux coupling in cases (iii) and (iv) can be realized through analytical estimations of the respective phoretic velocities based on leading order approximations and examining the contrast in the induced fluid flow. We estimate phoretic velocities for the Janus distribution of ionic flux and surface charge using densities of the form $\sim(1 \pm \cos\theta)$, as it accounts for the leading monopolar and dipolar contributions [17–19]. In the near-equilibrium DH regime, we find that the speeds of cases (iii) and (iv) can be expressed as $U_{(iii)} \approx [1 + \Delta(\kappa R)]U_{(i)}$ and $U_{(iv)} \approx [1 - \Delta(\kappa R)]U_{(i)}$, where $\Delta(x) = 2(x + 1)/(x^2 + 2x + 2)$ such that $0 < \Delta(\kappa R) < 1$. These analytical predictions, that are consistent with the numerical results obtained from FE simulations as shown in Fig. 3(b), capture the amplifying and diminishing effects in cases (iii) and (iv), which lead to the respective shifts in speeds. Case (iii) [case (iv)] has aligning [opposing] leading velocity contributions that amplify [diminish] speed and can be enhanced up to twofold compared to case (i) or (ii). Furthermore, Figs. 3(c) and 3(d) show the resulting fluid flow in the particle's rest frame for cases (iii) and (iv), respectively. Here we find that around the particle going from the moving front to the tail end, the fluid velocity increases in case (iii) and decreases in case (iv). This indicates the amplifying and diminishing effects emerging from the ion flux and surface charge interactions that direct the fluid around the particle induce faster and slower self-propulsion in the respective cases.

IV. CONCLUSION

In this article we show that surface charge asymmetry in chemically active colloids provides an alternative mechanism through which a local ionic gradient is generated to induce self-propulsion. In regimes where the particle size is smaller than or comparable to Debye length, the near-field electrostatics and hydrodynamics play a crucial role in facilitating the self-phoretic motion that arises from surface charge asymmetry, even when the ionic flux on the surface is uniform. The coupling of surface charge and ion flux asymmetries in

Janus nanoparticles, with nonvanishing surface charge and ion flux placed on opposite hemispheres, leads to significantly enhanced phoretic speeds in the order of μm/s or higher.

Our work focuses on the steady state behavior of the particle where it maintains propulsive motion. Beyond steady state regimes at longer timescales, Brownian and stochastic dynamics is expected to affect the particle's orientation and overall motion. The propulsion induced by surface asymmetries in active particles can lead to an enhanced Brownian motion at longer times [10,12,39,40]. Recent experiments [27,28] report charged nanomotors that release ions have been observed to exhibit a momentary burst of directed motion in between each random reorientation, reaching very fast ballistic speeds. However, a quantitative description for the long time behavior of such nanoparticles remains to be seen.

Taken together, our results suggest an additional mode to enhance phoretic self-propulsion of active nanoparticles in ionic media. This alternative avenue for optimization can be utilized in the design of nanomotors. Moreover, the analysis we provide here can lend some insight into the underlying mechanism behind transport and function of subcellular compartments with heterogeneous surface properties.

APPENDIX A: GENERALIZED LORENTZ RECIPROCAL THEOREM FOR STOKES FLOW

In this section we describe the Lorentz reciprocal theorem for Stokes flow that connects the solutions of two different Stokes problems. This method allows us to use the solution of a different Stokes problem that is already known to obtain the particle propulsion velocity for our problem at the steady state. The general Stokes equations are $\vec{\nabla} \cdot \boldsymbol{\sigma} + \vec{f} = 0$ and $\vec{\nabla} \cdot \vec{v} = 0$, where the fluid stress tensor $\boldsymbol{\sigma} = -p\boldsymbol{I} + \eta[\nabla\boldsymbol{v} + (\nabla\boldsymbol{v})^\dagger]$ and the body force density is $\vec{f}$. The Lorentz reciprocal theorem of Stokes flow when generalized for a nonvanishing body force states that

$$\int_S \hat{n} \cdot \boldsymbol{\sigma}^{(1)} \cdot \vec{v}^{(2)}\, dS - \int_V \vec{f}^{(1)} \cdot \vec{v}^{(2)}\, dV$$
$$= \int_S \hat{n} \cdot \boldsymbol{\sigma}^{(2)} \cdot \vec{v}^{(1)}\, dS - \int_V \vec{f}^{(2)} \cdot \vec{v}^{(1)}\, dV, \quad \text{(A1)}$$

where $(\vec{v}^{(1)}, \boldsymbol{\sigma}^{(1)})$ are the solutions to Problem 1 with body force $\vec{f}^{(1)}$, and $(\vec{v}^{(2)}, \boldsymbol{\sigma}^{(2)})$ are the solutions to Problem 2 with body force $\vec{f}^{(2)}$, as illustrated in Fig. 4, where both problems share the same geometry but are constrained to different body forces and drift speeds. In Eq. (A1), $\hat{n}$ is the unit vector pointing out of the particle surface S into the fluid domain of volume V.

Here we take Problem 1 to be the classic Stokes problem with zero body force $\vec{f}^{(1)} = 0$ for a sphere of radius R moving with constant velocity $U^{(1)}$ in the $\hat{z}$ direction [45]. Problem 2 is our problem of ionic self-diffusiophoresis with nonzero
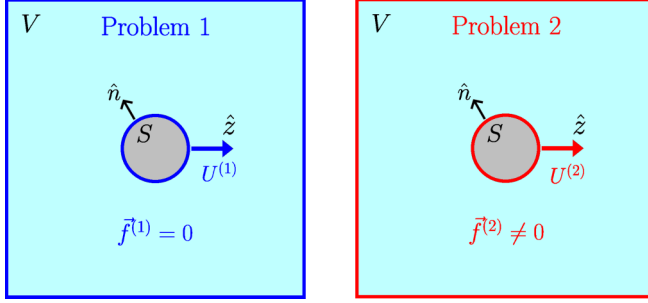
FIG. 4. Lorentz reciprocal theorem for Stokes flow. Schematic for Problem 1 of the classic Stokes problem with zero body force (left panel) and Problem 2 of ionic self-diffusiophoresis with electrostatic body force (right panel). Both for a spherical particle of radius R inside a fluid volume V.

electrostatic body force $\vec{f}^{(2)}$ for a sphere of radius R moving at steady state velocity $U^{(2)}\hat{z}$. In this setting the second term on the left-hand side of Eq. (A1) drops out, and using the no-slip boundary conditions at the surface for each problem and turning the first term on the right-hand side to a volume integral through Gauss's divergence theorem, we find

$$\vec{F}^{(1)} \cdot U^{(2)}\hat{z} = \int_V \vec{f}^{(2)} \cdot (U^{(1)}\hat{z} - \vec{v}^{(1)}) \, dV, \qquad \text{(A2)}$$

where we have for Problem 2 the body force $\vec{f}^{(2)} = \varepsilon \nabla^2 \psi \vec{\nabla} \psi$, and for Problem 1 the Stokes drag force $\vec{F}^{(1)} = -6\pi \eta R U^{(1)}\hat{z}$ and the solution of the fluid velocity $\vec{v}^{(1)} = U^{(1)}\hat{v}(r,\theta)$, with

$$\hat{v} = \left(\frac{3R}{2r} - \frac{R^3}{2r^3}\right)\cos\theta\hat{r} - \left(\frac{3R}{4r} + \frac{R^3}{4r^3}\right)\sin\theta\hat{\theta}. \qquad \text{(A3)}$$

We obtain our steady state propulsion speed $U^{(2)} = U$ given by Eq. (3) in the main text. We write the expression for U here explicitly in spherical coordinates with azimuthally symmetric $\psi(r,\theta)$,

$$U = \frac{\varepsilon}{3\eta R} \int_0^\pi \int_R^\infty \nabla^2 \psi \left[\frac{\partial \psi}{\partial r}\left(\frac{3Rr}{2} - \frac{R^3}{2r} - r^2\right)\cos\theta\sin\theta \right.$$
$$\left. - \frac{\partial \psi}{\partial \theta}\left(\frac{3R}{4} + \frac{R^3}{4r^2} - r\right)\sin^2\theta \right] dr d\theta. \qquad \text{(A4)}$$

We first note here that if ψ has no θ dependence then $U = 0$, since in this case all the remaining nonvanishing terms in Eq. (A4) are accompanied with the integral $\int_0^\pi \cos\theta\sin\theta d\theta$, which is identically zero. This method solves the hydrodynamic part of our problem and we are now left with having to solve for ψ, which is coupled to C_i thorough Eq. (1).

APPENDIX B: PERTURBATION EXPANSION IN THE DH LIMIT

In this section we carry out a perturbation expansion in the limit of small ion fluxes and small surface charge, and approximate an analytical expression for the steady state propulsion speed in such a regime. For the ions being produced at the particle surface, we perturb our system away from equilib-

rium state in the limit of small ion production rate I and low charge Q. To obtain the dimensionless equations, we first employ the transformations $r \to R\tilde{r}$, $\psi \to k_B T\tilde{\psi}/e$, and $C_\pm \to C_\infty \tilde{C}_\pm/2$, and now Eq. (1) reduces to

$$\nabla^2 \tilde{\psi} = \bar{\kappa}^2(\tilde{\psi} - \tilde{\rho}), \qquad \text{(B1)}$$

$$\nabla^2 \tilde{c} + \vec{\nabla}(\tilde{\rho}\vec{\nabla}\tilde{\psi}) = 0, \qquad \text{(B2)}$$

$$\nabla^2 \tilde{\rho} + \vec{\nabla}(\tilde{c}\vec{\nabla}\tilde{\psi}) = 0, \qquad \text{(B3)}$$

where the dimensionless Debye parameter $\bar{\kappa} = \kappa R$, and dimensionless fields $\tilde{c} = (\tilde{C}_+ + \tilde{C}_-)/2$ and $\tilde{\rho} = (\tilde{C}_+ - \tilde{C}_-)/2$. The dimensionless boundary conditions at the particle surface become

$$-\vec{\nabla}\tilde{\psi} \cdot \hat{r} \, |_{\tilde{r}=1} = \delta_Q \tilde{\sigma}(\theta), \qquad \text{(B4)}$$

where the dimensionless parameter quantifying the surface charge $\delta_Q = eQ/4\pi R\varepsilon k_B T$. For the ion concentrations, we have $-(\vec{\nabla}\tilde{C}_\pm \pm \tilde{C}_\pm\vec{\nabla}\psi) \cdot \hat{r} \, |_{\tilde{r}=1} = \delta_{I\pm}\tilde{j}(\theta)$, where the dimensionless parameter quantifying ion fluxes $\delta_{I\pm} = I_\pm/2\pi RC_\infty D_\pm$ of the particle. Writing in terms of $\tilde{c}$ and $\tilde{\rho}$, we get

$$-(\vec{\nabla}\tilde{c} + \tilde{\rho}\vec{\nabla}\psi) \cdot \hat{r} \, |_{\tilde{r}=1} = \delta_I \tilde{j}(\theta), \qquad \text{(B5)}$$

$$-(\vec{\nabla}\tilde{\rho} + \tilde{c}\vec{\nabla}\psi) \cdot \hat{r} \, |_{\tilde{r}=1} = \delta_I \beta \tilde{j}(\theta), \qquad \text{(B6)}$$

where $\beta = (D_- - D_+)/(D_- + D_+)$ and $\delta_I = I(D_- + D_+)/8\pi RC_\infty D_+ D_-$. We now have the perturbation expansions in the order of δ_I and δ_Q as

$$\tilde{\psi} = \delta_Q \tilde{\psi}_0 + \delta_I \tilde{\psi}_1 + \mathcal{O}[\delta_I^2, \delta_Q^2, \delta_I \delta_Q], \qquad \text{(B7)}$$

$$\tilde{c} = \delta_I \tilde{c}_0 + \mathcal{O}[\delta_I^2, \delta_I \delta_Q], \qquad \text{(B8)}$$

$$\tilde{\rho} = \delta_I \tilde{\rho}_0 + \mathcal{O}[\delta_I^2, \delta_I \delta_Q]. \qquad \text{(B9)}$$

This corresponds to an expansion of the dimensionless speed as

$$\tilde{U} = \delta_I \delta_Q \tilde{U}_0 + \delta_I^2 \tilde{U}_1 + \delta_Q^2 \tilde{U}_2 + \mathcal{O}[\delta_I^2 \delta_Q, \delta_I \delta_Q^2],$$

such that $U = \varepsilon k_B^2 T^2 \tilde{U}/6\pi \eta Re^2$ and the leading order contributions as given by

$$\tilde{U}_0 = \bar{\kappa}^2 \int_{\tilde{V}} ((\tilde{\psi}_1 - \tilde{\rho}_0)\vec{\nabla}\tilde{\psi}_0 + \tilde{\psi}_0\vec{\nabla}\tilde{\psi}_1) \cdot (\hat{v} - \hat{z}) \, d\tilde{V}, \quad \text{(B10)}$$

$$\tilde{U}_1 = \bar{\kappa}^2 \int_{\tilde{V}} (\tilde{\psi}_1 - \tilde{\rho}_0)\vec{\nabla}\tilde{\psi}_1 \cdot (\hat{v} - \hat{z}) \, d\tilde{V}, \qquad \text{(B11)}$$

$$\tilde{U}_2 = \bar{\kappa}^2 \int_{\tilde{V}} \tilde{\psi}_0\vec{\nabla}\tilde{\psi}_0 \cdot (\hat{v} - \hat{z}) \, d\tilde{V}. \qquad \text{(B12)}$$

We now plug in the expansion equations, Eqs. (B7)–(B9), into Eqs. (B1) and (B3), as well as into the boundary conditions, Eqs. (B4) and (B6). Then, by collecting the terms with same coefficients, we find that $\tilde{\psi}_0$, $\tilde{\rho}_0$, and $\tilde{\psi}_1$ satisfy the following equations:

$$\nabla^2 \tilde{\psi}_0 = \bar{\kappa}^2 \tilde{\psi}_0, \qquad \text{(B13)}$$

$$\nabla^2 \tilde{\rho}_0 = 0, \qquad \text{(B14)}$$

$$\nabla^2 \tilde{\psi}_1 = \bar{\kappa}^2(\tilde{\psi}_1 - \tilde{\rho}_0), \qquad \text{(B15)}$$

and boundary conditions

$$-\vec{\nabla}\tilde{\psi}_0 \cdot \hat{r}\,|_{\tilde{r}=1} = \tilde{\sigma}(\theta), \tag{B16}$$

$$-\vec{\nabla}\tilde{\rho}_0 \cdot \hat{r}\,|_{\tilde{r}=1} = \beta\tilde{j}(\theta), \tag{B17}$$

$$-\vec{\nabla}\tilde{\psi}_1 \cdot \hat{r}\,|_{\tilde{r}=1} = 0. \tag{B18}$$

In this limit we find that the leading order phoretic speed can be obtained by solving, firstly, Eqs. (B13) and (B14), which are the DH and Laplace equations in spherical coordinates, respectively.

APPENDIX C: ANALYTICAL SOLUTIONS TO THE DH AND LAPLACE EQUATIONS IN SPHERICAL COORDINATES

In spherical coordinates with azimuthal symmetry, through the separation of variables method [46] we find the general solution to Eq. (B13),

$$\tilde{\psi}_0(r,\theta) = \sum_{n=0}^{\infty} A_n\, k_n(\bar{\kappa}r)\, P_n(\cos\theta), \tag{C1}$$

where k_n are the modified spherical Bessel functions and P_n are the Legendre polynomials. Applying boundary condition Eq. (B16) gives the coefficients,

$$A_n = \frac{1}{\bar{\kappa}\,k_{n+1}(\bar{\kappa}) - n\,k_n(\bar{\kappa})} \int_0^{\pi} \tilde{\sigma}(\theta) P_n(\cos\theta) \sin\theta\, d\theta. \tag{C2}$$

Similarly, we get the general solutions for Eq. (B14),

$$\tilde{\rho}_0(r,\theta) = \sum_{n=0}^{\infty} B_n\, r^{-(n+1)}\, P_n(\cos\theta) \tag{C3}$$

with

$$B_n = \frac{\beta}{(n+1)} \int_0^{\pi} \tilde{j}(\theta) P_n(\cos\theta) \sin\theta\, d\theta. \tag{C4}$$

Using the solution Eq. (C3), we can solve Eq. (B3) with boundary condition Eq. (B18). We focus here on the case of asymmetric surface charge $\tilde{\sigma}(\theta) = 1 \pm \cos\theta$ and uniform ion flux $\tilde{j}(\theta) = 1$, which reduces Eq. (C1) to the monopole ($n = 0$) and dipole ($n = 1$) terms and Eq. (C3) to only the monopole term ($n = 0$). In this case we find that the contribution of the order δ_I^2 as well as δ_Q^2 vanishes, that is, we get $\tilde{U}_1 = 0$ and $\tilde{U}_2 = 0$. Thus, in this case only $\delta_I\delta_Q$ order contribution remains as the leading term. We arrive at the leading order velocity given by Eqs. (4) and (5) in the main text.

APPENDIX D: LIMITING CASES OF κR

Additionally, we look at the two limiting case of the phoretic speed. First, when the size of the particle is small compared to the Debye length $1/\kappa$, i.e., the thick Debye layer limit, and then conversely, when the size of the particle is large compared to the Debye length, i.e., the thin Debye layer limit. On one hand, if we expand our leading order velocity given by Eqs. (3) and (4) in the main text for small $\kappa R \ll 1$, we
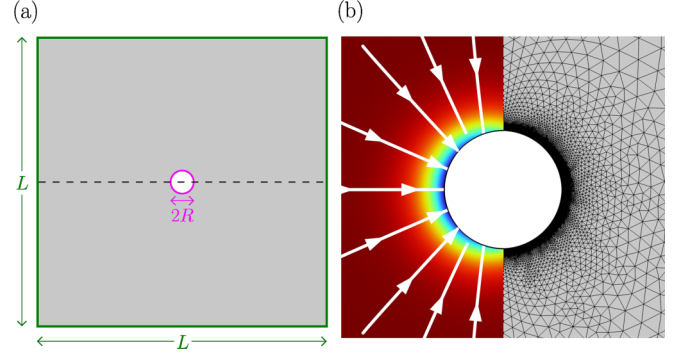

FIG. 5. Schematic of the COMSOL simulations for ionic self-diffusiophoresis. (a) The *2D axisymmetric* cross-sectional geometry with a circle for the particle of radius R placed at the center of a $L \times L$ rectangle enclosing the fluid solution region. The dashed line indicates the axis of symmetry, and we use $L \approx 100\,R$ in our simulations. (b) Mesh size variation near the particle surface (right side) and the corresponding solution of the electric potential that is shown in Fig. 2 of the main text (left side). We vary the mesh from a finer size of $0.0001\,R$ to a sparser size of $0.1\,R$ progressing radially outwards.

find

$$|U_{\sigma\pm}| \approx \frac{|\alpha I Q|}{48R}\left(1 - \frac{8}{3}\kappa R + 2[1 - \gamma - \ln(\kappa R)](\kappa R)^2\right), \tag{D1}$$

where γ is the Euler-Mascheroni constant. We see that in this limit it acquires larger speeds, and the magnitude of the propulsion speed scales as $|U_{\sigma\pm}| \sim |IQ\alpha|/48R$ in the DH approximation. On the other hand, if we expand our leading order velocity given by Eqs. (3) and (4) in the main text for large $\kappa R \gg 1$, we find $|U_{\sigma\pm}| \approx |\alpha I Q|/3R(\kappa R)^4$. In this limit we instead see that the particle approaches zero speed.

APPENDIX E: NUMERICAL SIMULATIONS IN COMSOL

In this section we detail the setup of our numerical simulations done in COMSOL. The finite element numerical simulations are carried out via COMSOL MULTIPHYSICS software [47] performed in the particle's rest (or comoving) frame of reference at steady state. Due to the azimuthal symmetry of the particle-solution system, our simulations entail a *2D axisymmetric* setup in COMSOL with a cross-sectional geometry consisting of a circular region of radius R at the center of a rectangular region of dimensions $L \times L$ where we set $L \approx 100\,R$ [see Fig. 5(a)]. We employ a *Multiphysics* interface coupling in COMSOL between the *Electrostatics* (*es*) and the *Transport of Diluted Species* (*tds*) interfaces provided by the *Chemical Reaction Engineering* module, in conjunction with the *Creeping Flow* (*spf*) interface provided by the *Computational Fluid Dynamics* module. This setup amounts to numerically solving the fully coupled Poisson-Nernst-Planck-Stokes equations at steady state, namely, Eqs. (1) and (2), in the fluid region enclosed between the circle and the rectangle. We implement the particle surface boundary conditions (A) at the circumference of the circle, and the bulk conditions (B) are applied at the edges of the rectangle. However, since we
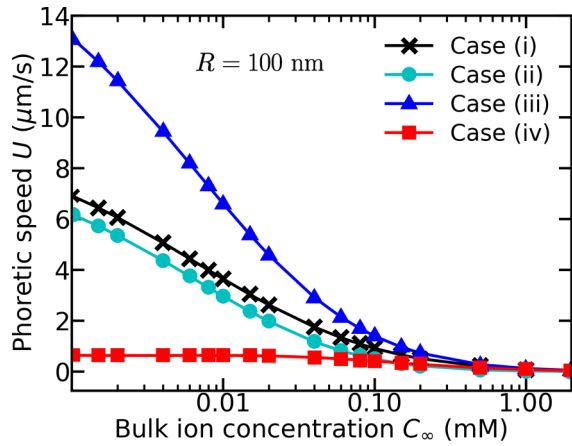
FIG. 6. Phoretic speed as a function of bulk ion concentration for the different surface charge and ion flux configurations, cases (i)–(iv), as in Fig. 3 of main text but for a larger particle size of $R = 100$ nm.

are in the particle's rest frame, the boundary conditions given in (B) are transformed into $\vec{v}\,|_{r=R} = 0$ and $\vec{v}\,|_{r\to\infty} = -U\hat{z}$, respectively.

Near the particle-solution boundary, that is, closer to the circle in our simulation, a finer mesh is required. In accordance with the geometry of our system, we radially vary our mesh size, increasing from $0.0001\,R$ to $1\,R$ in our bounded domain, with the finer mesh near the circumference and the sparser mesh away from it until the edge [see Fig. 5(b)]. Such a meshing yields a convergent solution of the electric potential, ion concentration, and fluid velocity for the relevant ranges of parameter values. We then iteratively solve for the value of U such that the net force on the particle is zero and obtain the plot data for the phoretic speed as a function of the adjustable parameters such as bulk ion concentration.

APPENDIX F: LARGER NANOPARTICLE SIZE

We illustrate here in Fig. 6 speeds for the four scenarios of the surface charge and ion flux configurations as discussed and shown in Fig. 3 of the main text but for a larger particle size. In contrast to smaller nanoparticles, we find that larger ones move with lower speeds and maintain directed propulsion at a regime of lower bulk ion concentration. For instance, compared to the particle of $R = 20$ nm in the main text, a particle with $R = 100$ nm obtains optimal speeds of up to ~ 10 µm/s but at much lower bulk concentrations ~ 0.001 mM and sustains nonvanishing speeds only up to ~ 1 mM. Although prevalent in a very low bulk concentration regime, we preserve the same behavior in larger particles with regard to the effect of surface configurations, as the case (iii) still yields the largest propulsion speeds. Hence the particle size plays a critical role here, as our results indicate that smaller nanoparticles maximize transport speeds that span a larger range of bulk ion concentrations.

[1] D. Bray, *From Molecules to Motility*, 2nd ed. (Garland Science Publishing, New York City, 2000).

[2] E. Lauga and T. R. Powers, Rep. Prog. Phys. **72**, 096601 (2009).

[3] J. L. Moran and J. D. Posner, Annu. Rev. Fluid Mech. **49**, 511 (2017).

[4] W. Gao and J. Wang, Nanoscale **6**, 10486 (2014).

[5] L. Soler and S. Sánchez, Nanoscale **6**, 7175 (2014).

[6] J. L. Anderson, Annu. Rev. Fluid Mech. **21**, 61 (1989).

[7] D. Velegol, A. Garg, R. Guha, A. Kar, and M. Kumar, Soft Matter **12**, 4686 (2016).

[8] S. Ebbens, Curr. Opin. Colloid Interface Sci. **21**, 14 (2016).

[9] A. Zöttl and H. Stark, J. Phys.: Condens. Matter **28**, 253001 (2016).

[10] P. Illien, R. Golestanian, and A. Sen, Chem. Soc. Rev. **46**, 5508 (2017).

[11] R. Golestanian, T. B. Liverpool, and A. Ajdari, Phys. Rev. Lett. **94**, 220801 (2005).

[12] R. Golestanian, T. B. Liverpool, and A. Ajdari, New J. Phys. **9**, 126 (2007).

[13] J. Zhang, B. A. Grzybowski, and S. Granick, Langmuir **33**, 6964 (2017).

[14] S. Ebbens, D. A. Gregory, G. Dunderdale, J. R. Howse, Y. Ibrahim, T. B. Liverpool, and R. Golestanian, Europhys. Lett. **106**, 58003 (2014).

[15] Y. Ibrahim, R. Golestanian, and T. B. Liverpool, J. Fluid Mech. **828**, 318 (2017).

[16] C. Zhou, H. P. Zhang, J. Tang, and W. Wang, Langmuir **34**, 3289 (2018).

[17] M. De Corato, X. Arqué, T. Patiño, M. Arroyo, S. Sánchez, and I. Pagonabarraga, Phys. Rev. Lett. **124**, 108001 (2020).

[18] E. S. Asmolov, T. V. Nizkaya, and O. I. Vinogradova, Phys. Fluids **34**, 032011 (2022).

[19] A. T. Brown, W. C. K. Poon, C. Holm, and J. de Graaf, Soft Matter **13**, 1200 (2017).

[20] X. Zhou, S. Wang, L. Xian, Z. H. Shah, Y. Li, G. Lin, and Y. Gao, Phys. Rev. Lett. **127**, 168001 (2021).

[21] S. Hermanová and M. Pumera, Chem. Euro. J. **26**, 11085 (2020).

[22] M. Safdar, S. U. Khan, and J. Jänis, Adv. Mater. **30**, 1703660 (2018).

[23] A. I. Campbell, S. J. Ebbens, P. Illien, and R. Golestanian, Nat. Commun. **10**, 3952 (2019).

[24] B. Ramm, A. Goychuk, A. Khmelinskaia, P. Blumhardt, H. Eto, K. A. Ganzinger, E. Frey, and P. Schwille, Nat. Phys. **17**, 850 (2021).

[25] R. P. Sear, Phys. Rev. Lett. **122**, 128101 (2019).

[26] I. Santiago, Nano Today **19**, 11 (2018).

[27] T.-C. Lee, M. Alarcón-Correa, C. Miksch, K. Hahn, J. G. Gibbs, and P. Fischer, Nano Lett. **14**, 2407 (2014).

[28] J. Sun, M. Mathesh, W. Li, and D. A. Wilson, ACS Nano **13**, 10191 (2019).

[29] M. Sutter, M. R. Melnicki, F. Schulz, T. Woyke, and C. A. Kerfeld, Nat. Commun. **12**, 3809 (2021).

[30] C. A. Kerfeld, M. R. Sawaya, S. Tanaka, C. V. Nguyen, M. Phillips, M. Beeby, and T. O. Yeates, Science **309**, 936 (2005).

[31] C. Fan, S. Cheng, Y. Liu, C. M. Escobar, C. S. Crowley, R. E. Jefferson, T. O. Yeates, and T. A. Bobik, Proc. Natl. Acad. Sci. USA **107**, 7509 (2010).

[32] E. Mallette and M. S. Kimber, J. Biol. Chem. **292**, 1197 (2017).

[33] M. Sutter, T. G. Laughlin, N. B. Sloan, D. Serwas, K. M. Davies, and C. A. Kerfeld, Plant Physiol. **181**, 1050 (2019).

[34] M. Sommer, F. Cai, M. Melnicki, and C. A. Kerfeld, J. Exp. Bot. **68**, 3841 (2017).

[35] S. Li, D. A. Matoz-Fernandez, and M. Olvera de la Cruz, ACS Nano **15**, 14804 (2021).

[36] J. Steinkühler, C. H. Abrahamson, J. Agudo-Canalejo, R. Golestanian, D. Tullman-Ercek, and N. P. Kamat, bioRxiv 2022.05.16.492142.

[37] J. L. Moran and J. D. Posner, J. Fluid Mech. **680**, 31 (2011).

[38] E. Yariv, Proc. R. Soc. Ser. A. **467**, 1645 (2011).

[39] R. Golestanian, Phys. Rev. Lett. **102**, 188305 (2009).

[40] J. R. Howse, R. A. L. Jones, A. J. Ryan, T. Gough, R. Vafabakhsh, and R. Golestanian, Phys. Rev. Lett. **99**, 048102 (2007).

[41] H. Masoud and H. A. Stone, J. Fluid Mech. **879**, P1 (2019).

[42] H. A. Stone and A. D. T. Samuel, Phys. Rev. Lett. **77**, 4102 (1996).

[43] J. Happel and H. Brenner, *Low Reynolds Number Hydrodynamics* (Springer, Netherlands, 1983).

[44] A. Domínguez, M. N. Popescu, C. M. Rohwer, and S. Dietrich, Phys. Rev. Lett. **125**, 268002 (2020).

[45] L. Landau and E. Lifshitz, *Fluid Mechanics*, 2nd ed. (Pergamon, New York, 1987).

[46] G. B. Arfken, H. J. Weber, and F. E. Harris, *Mathematical Methods for Physicists*, 7th ed. (Academic Press, New York, 2012).

[47] COMSOL Multiphysics v. 6.0, COMSOL AB, Stockholm, Sweden, www.comsol.com.